

Static Test and Seismic Dynamic Response of an Innovative 3D Seismic Isolation System

Wenguang Liu¹; Hao Xu²; Wenfu He³; and Qiaorong Yang⁴

Abstract: Seismic isolation is an efficient strategy to protect structures from the effects of moderate to severe earthquake shaking. Conventional isolation devices can reduce the structural response in horizontal directions only; however, three-dimensional (3D) ground motions have been observed in earthquake records. In this paper, an innovative 3D seismic isolator is proposed. A new kind of asymmetric oblique hysteretic model is illustrated, and a quasistatic compression test of a model device using three lead rubber bearings (LRBs) is conducted. The test results and theoretical model results match well. A significant asymmetric property is observed in the hysteretic curves. The proposed hysteretic model can efficiently simulate the vertical mechanical behavior of a 3D seismic isolation system. The effects of different parameters are highlighted based on the theoretical mechanical model. The inclination angle, friction coefficient, and second shape factor of the inclined LRBs strongly influence the vertical behavior of the proposed device. A dynamic response analysis of the substructure of a nuclear power plant (NPP) is conducted. The hysteretic curves have the shape of an asymmetric quadrangle; this shape is similar to that observed in the test results. The vertical acceleration response of the vertical isolation structure is reduced by 33% compared with that of a fixed-base structure and reduced by 58% compared with that of a horizontal isolation structure. The proposed 3D isolator can sufficiently isolate the seismic input.

DOI: [10.1061/\(ASCE\)ST.1943-541X.0002195](https://doi.org/10.1061/(ASCE)ST.1943-541X.0002195). © 2018 American Society of Civil Engineers.

Author keywords: Three-dimensional (3D) isolation; Lead rubber bearing; Frictional sliding; Asymmetric hysteretic model; Static test; Dynamic analysis.

Introduction

The basic concept of seismic base isolation is to introduce a flexible layer between the base floor and foundation to reduce damage to the superstructure during earthquake ground motions. It has been proven an efficient method to reduce earthquake disaster (Liu 2003). Earthquakes are complex and random, shaking the ground in three directions. However, vertical earthquakes are usually underestimated (Papazoglou and Elnashai 1996). Generally, the maximum acceleration of vertical motion is 1/2–1/3 smaller than that of horizontal motion (Architectural Society of Japan 2006). In the Chinese design code, vertical ground motions must be taken into account only in regions with a seismic design-basis intensity of 9°, and the vertical earthquake load is considered only 65% of the horizontal load (UDC 2010). The seismic intensity mentioned here is the Mercalli earthquake intensity; an earthquake that may occur within the next 50 years has a 10% probability of being more intense than the design-basis seismic intensity. However, strong vertical ground motions and structural damage have been observed across the world (Papazoglou and Elnashai 1996). A vertical acceleration of 1.25 g was observed during the San Fernando earthquake in 1971 (Bertero et al. 1978). The El Centro station recorded a vertical acceleration of

1.655 g during the Imperial Valley earthquake in the United States in 1971, and the ratio of vertical to horizontal acceleration (V/H) reached 3.77 (Chopra 2005). Extensive structural damage caused by vertical ground motions due to the Kalamata earthquake in Greece, 1968; Northridge earthquake in the United States, 1994; and Kobe earthquake in Japan, 1995, was observed (Papazoglou and Elnashai 1996). During the Northridge earthquake, the peak vertical acceleration was 1.18 g and the V/H ratio was 1.69 (Papazoglou and Elnashai 1996), as is shown in Table 1. Large vertical accelerations, some of which were even larger than the corresponding horizontal accelerations, were recorded during the Kobe earthquake in Japan, 1995 (Bozorgnia et al. 2000); Chi-Chi earthquake in Taiwan, 1999 (Xue 2000); Bam earthquake in Iran, 2003 (Hossein and Kabeyasawa 2004); Niigata-ken Chuetsu earthquake in Japan, 2004 (Yang and Lee 2007); and Wenchuan earthquake in China, 2008 (Li et al. 2008). Conventional seismic isolation systems are not designed to reduce the structural response in the vertical direction. Sometimes these systems even amplify vertical responses. Therefore, research on three-dimensional (3D) seismic isolation is necessary.

The devices installed in the base of a structure need to support the superstructure, and seismic isolation requires low vertical stiffness. The desire for a high bearing capacity conflicts with the low vertical stiffness of isolation systems; this is the main difficulty in realizing 3D isolation.

A new 3D isolation system was put forward by Fujita et al. (1996), in which disc springs were used for vertical isolation and rubber bearings were used for horizontal isolation. The retrofitting of the Pestalozzi school in Yugoslavia using thick rubber bearings was the first application of the 3D isolation system (Garevski et al. 2000). A hydraulic cylinder system with a rocking suppression device was proposed by Kato et al. (2002) and Sawa et al. (2002). Research on thick rubber bearings, air springs, and hydraulic cylinders was conducted by Yabana and Matsuda (2000) and Morishita et al. (2004). A device that included metal bellows in the vertical

¹Professor, Dept. of Civil Engineering, Shanghai Univ., Shanghai 200444, China (corresponding author). Email: 13791980@qq.com

²Ph.D. Student, Dept. of Civil Engineering, Shanghai Univ., Shanghai 200444, China. Email: xuhaoy08@163.com

³Associate Professor, Dept. of Civil Engineering, Shanghai Univ., Shanghai 200444, China. Email: howunfu@shu.edu.cn

⁴Associate Professor, Dept. of Civil Engineering, Shanghai Univ., Shanghai 200444, China. Email: yangqr@aliyun.com

Note. This manuscript was submitted on November 30, 2016; approved on May 8, 2018; published online on September 19, 2018. Discussion period open until February 19, 2019; separate discussions must be submitted for individual papers. This paper is part of the Journal of Structural Engineering, © ASCE, ISSN 0733-9445.

Table 1. Northridge earthquake records possessing a strong vertical component data

Station	Epicentral distance (km)	Vertical PGA (g)	Horizontal PGA (g)	V/H
Tarzana, Cedar Hill Nursery	5	1.18	1.82	0.65
Arleta, Nordhoff Avenue Fire Station	10	0.59	0.35	1.69
Sylmar, County Hospital	16	0.60	0.91	0.66
Newhall, LA County Fire Station	20	0.62	0.63	0.98

direction and rubber bearing in the horizontal direction was proposed by Ogiso et al. (2003). Metal bellows are a combination of a metal damper and air spring and can support the superstructure and dissipate energy. Development of 3D seismic isolation technology for the next generation of nuclear power plants (NPPs) in Japan was introduced by Masaki et al. (2003) and Inoue et al. (2004). The performance requirements for a 3D isolation system and the developing targets for 3D isolation technology were illustrated. A shaking table test of a rolling seal-type air spring system was conducted by Suhara et al. (2004). A nonlinear spring mechanism consisting of an A-shaped link, coil springs, and a linear guide was proposed by Ueda et al. (2007). This new device has approximate bilinear-type mechanical properties. An innovative 3D isolation system placed under the Herculaneum Roman Ship was designed, and a shaking table test was conducted by Indirli et al. (2009). Experiments on 1/2-scale hydraulic springs with a rocking suppression device and seismic simulation on a full-scale building were conducted by Shimada et al. (2010). A novel 3D isolation system consisting of disc springs, a metal damper, and a rubber bearing was proposed by Ou and Jia (2010), and the seismic behavior of an isolated continuous bridge was explored. A device consisting of an air spring, a rubber bearing, and a sliding rail was established in a 3-story reinforced concreted (RC) apartment building in Tokyo (Tomizawa et al. 2012). This was the first newly built construction project that applied 3D isolation technology in the world. A shaking table test of a system composed of wedge-shaped friction blocks and springs was conducted by Lee et al. (2014). Research on distributed flexibility and damping strategy was conducted by Vu et al. (2014). The properties of existing 3D isolation systems and their potential applications to modern nuclear facilities were discussed by Zhou et al. (2016). Additionally, the appropriate vertical frequency was explored.

Design and Structure of New Device

In this paper, a new 3D oblique sliding friction seismic isolator (3D OSFSI) is proposed [W. G. Liu, H. Xu, et al., "Oblique sliding damping 3D seismic isolation device," Chinese Patent No. CN104481046A (2015)]. The device consists of a horizontal rubber bearing, a sliding block, friction blocks, inclined lead rubber bearings (LRBs), connection blocks, and restrainers. A sketch of the 3D OSFSI is shown in Fig. 1. The inclined LRBs are installed symmetrically in a circle. The number of inclined LRBs used can vary according to the design requirements. The restrainers are established to make the sliding block move up and down and transmit shear force from the superstructure to base, not to overburden the inclined LRBs. In an actual structure, restrainer can be steel sheets, vertical guide rails, or RC retaining walls.

Due to the inclination angle, the vertical load decomposes into slant components F_1 and F_2 . The vertical displacement transforms into compression-shear deformation of the inclined LRBs and

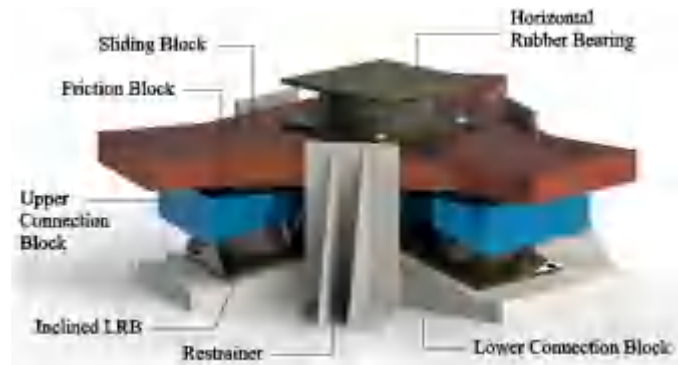


Fig. 1. 3D OSFSI.

frictional sliding of the friction blocks. A deformation and load sketch is shown in Fig. 2.

During an earthquake, vertical friction forces f develop between the restrainers and sliding block. In addition, the contact force N will be roughly equal to the lateral force of the isolator. Low-friction materials should be used at the contact surfaces so that the friction force will be too small to affect the vertical behavior of the 3D OSFSI ($f = \mu \cdot N$). Otherwise, the lateral deformation of the horizontal bearing would affect the vertical behavior, and the vertical behavior and horizontal behavior would be coupled.

Mechanical Model of 3D OSFSI

In this paper, the vertical compressive behavior of the 3D OSFSI is mainly investigated. The 3D OSFSI is a series system that consists of a horizontal rubber bearing and inclined LRBs. The contribution of the horizontal rubber bearing on the vertical stiffness is ignored because its vertical stiffness is much greater.

The mechanical properties of elastomeric bearings and LRBs have been systematically researched. Mechanical models and simulation methods of elastomeric bearings have been proposed by Haringx (1948), Kelly et al. (1987), and Chan and Kelly (1988). Nagarajaiah and Ferrell (1999) and Ryan et al. (2006) investigated the nonlinear properties and stability of elastomeric bearings and extended the two-spring model to consider material and geometric nonlinearity. Warn et al. (2007) explored different formulations for vertical stiffness and found that the tension-bulking theory results shows the best agreement with the test results. The nonlinear stiffness and stability of rubber bearings were explored by Warn and Whittaker (2008), Weisman and Warn (2012), Sanchez et al. (2013), and Han et al. (2013).

The horizontal postyield stiffness of LRBs under a compression-shear condition is (Haringx 1948)

$$K_{d0} = \frac{P^2}{2k_{rc}q \tan(\frac{\phi h}{2}) - ph} \quad (1)$$

$$q = \sqrt{k_{rc} \left(1 + \frac{P}{k_s} \right)} \quad (2)$$

where k_{rc} = bending stiffness of the elastomer; $k_{rc} = E_{rb}l$; k_s = shear stiffness, $k_s = GA$; P = vertical pressure; h = height of the elastomer; E_{rb} = compression modulus of the elastomer; G = shear modulus; A = section area; and l = section inertia moment.

Considering the influence of the lead core, the shear stiffness is (Architectural Society of Japan 2006)

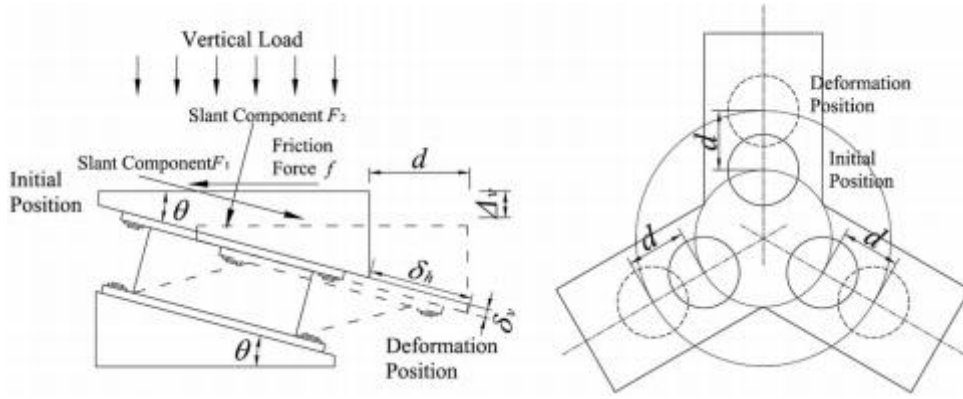


Fig. 2. Deformation and load sketch of the inclined LRBs.

$$K_{d0} = \frac{GA}{T_R} \left(1 + \alpha \frac{A_p}{A} \right) \quad (3)$$

$$K_{v0} = \frac{E_{cb} \cdot A}{T_R} \quad (6)$$

The shear stiffness of the bearing under a vertical load is (Kelly et al. 1987)

$$K_d = \left[1 - \left(\frac{\sigma}{\sigma_{cr}} \right)^2 \right] K_{d0} \quad (4)$$

$$\sigma_{cr} = \zeta GS_1 S_2 = \pi \sqrt{\frac{\kappa}{8(1+2\kappa S_1^2 G)} \cdot GS_1 S_2} \quad (5)$$

when the pressure and lateral deformation are both 0, the vertical stiffness is (Haringx 1948)

Considering the vertical pressure and lateral deformation, the vertical stiffness is (Warn et al. 2007)

$$K_v = K_{v0} \frac{1}{\left[1 + 3 \cdot \frac{\pi b - \sin(\pi b)}{1 - \cos(\pi b)} \cdot \left(\frac{\delta}{R} \right)^2 \right]} \quad (7)$$

The horizontal yielding load is

$$Q_d = \sigma_{pb} \cdot A_p \quad (8)$$

where G = shear modulus of the rubber; A = area of the rubber; A_p = area of the lead core; and α = correction coefficient of the lead core. When the shear strain is 50%, the value of α is 4. T_R = total thickness of the rubber sheets; σ = compressive stress of the LRB; σ_{cr} = bulking stress of the LRB; κ = correction coefficient; S_1 and S_2 = shape factors of the LRB; E_{cb} = compression modulus; and δ = lateral deformation. Additionally, R = radius of the LRB, $b = P = P_{cr}$, where P_{cr} = critical buckling load accounting for the shear deformation and is calculated according to $P_{cr} = \sigma_{cr} \cdot A$; and σ_{pb} = effective yield strength of the lead.

The hysteretic model of the 3D OSFSI is composed of the oblique compression model of the LRB, the oblique shear model of the LRB, and the Coulomb friction model. The friction force varies with displacement because the vertical force changes. Thus, a new kind of asymmetric oblique hysteretic model is introduced for the 3D OSFSI, as shown in Figs. 3 and 4. The postyield loading and unloading stiffness are different, and the hysteretic loop is asymmetric.

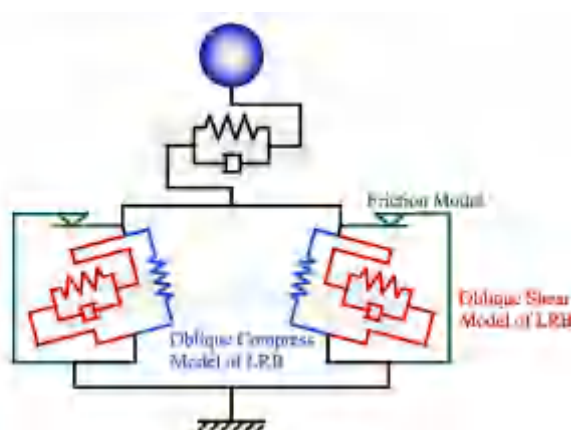


Fig. 3. Mechanical model of the proposed system.

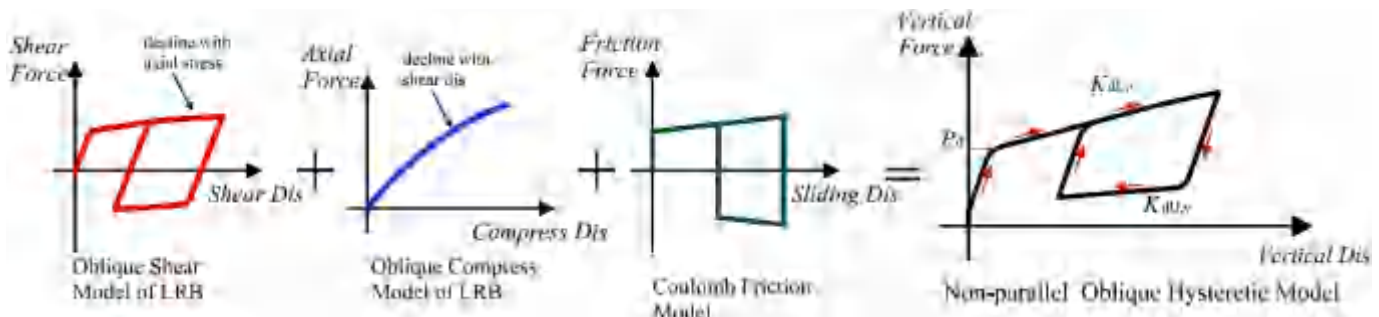


Fig. 4. Vertical hysteretic model of the 3D OSFSI.

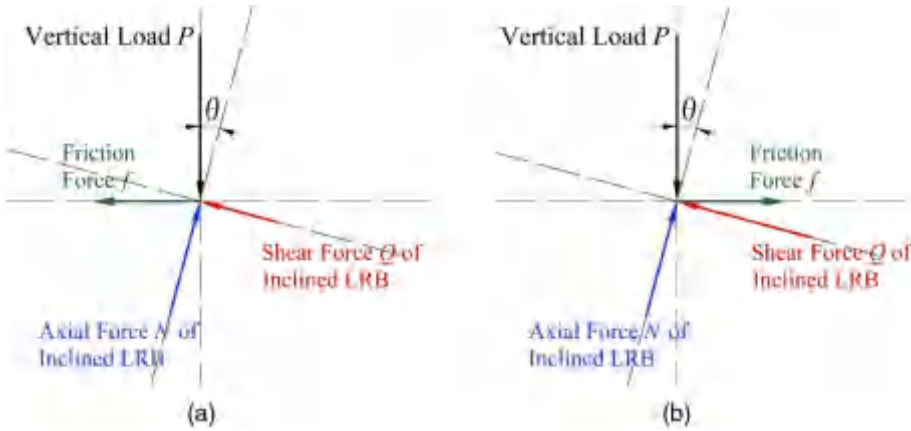


Fig. 5. Mechanical analysis of the inclined LRB: (a) loading process; and (b) unloading process.

The load condition of the inclined LRBs during the loading and unloading processes is shown in Fig. 5. The friction force reverses when the sliding direction changes.

The vertical stiffness of the 3D OSFSI is the ratio of the vertical load increment and vertical deformation increment

$$K_v = \frac{dP}{d\Delta_v} \quad (9)$$

The load condition during the load process is shown in Fig. 5(a). With the vertical load increment dP , the shear force increment dQ of the inclined LRB is

$$dQ = dP \cdot \sin \theta - df \cdot \cos \theta = dP \cdot (\sin \theta - \mu \cdot \cos \theta) \quad (10)$$

The shear deformation increment of the inclined LRB is

$$\delta_h = dQ = K_d \quad (11)$$

The axial force increment of the inclined LRB is

$$dN = dP \cdot \cos \theta + df \cdot \sin \theta \quad (12)$$

The axial deformation increment of the inclined LRB is

$$\delta_v = dN = K_v \quad (13)$$

The vertical deformation increment of the 3D OSFSI is

$$d\Delta_v = d\delta_h \cdot \sin \theta + d\delta_v \cdot \cos \theta \quad (14)$$

The vertical postyield load stiffness of 3D OSFSI is

$$K_{dL;V} = \frac{n \cdot dP}{d\Delta_v} = \frac{n \cdot K_d \cdot K_v}{K_v \cdot (\sin^2 \theta - \mu \cdot \sin \theta \cdot \cos \theta) + K_d \cdot (\cos^2 \theta + \mu \cdot \sin \theta \cdot \cos \theta)} \quad (15)$$

The vertical postyield loading stiffness of the 3D OSFSI is

$$P_d = \frac{n \cdot Q_d}{\sin \theta - \mu \cdot \cos \theta} \quad (16)$$

where μ = friction coefficient of the friction block and sliding block; n = number of the inclined LRBs; θ = inclination angle of the connection block; and K_d , K_v , and Q_d = horizontal postyield

stiffness, vertical stiffness, and horizontal yielding load of the inclined LRB, respectively.

The vertical postyield unloading stiffness of the 3D OSFSI can be obtained with the same method and is

$$K_{dU;V} = \frac{n \cdot dP}{d\Delta_v} = \frac{n \cdot K_d \cdot K_v}{K_v \cdot (\sin^2 \theta + \mu \cdot \sin \theta \cdot \cos \theta) + K_d \cdot (\cos^2 \theta - \mu \cdot \sin \theta \cdot \cos \theta)} \quad (17)$$

The preyield stiffness can be assumed to be 10–15 times the postyield stiffness (Architectural Society of Japan 2006).

Eqs. (15) and (17) show that the postyield loading and unloading stiffnesses are different

$$K_{dL;V} > K_{dU;V} \quad (18)$$

The postyield loading stiffness is larger than the unloading stiffness; this asymmetry is illustrated in Fig. 4. In addition, this asymmetry is the greatest difference between the proposed model of a 3D OSFSI and the traditional bilinear model of a LRB.

Vertical Compression Test

A vertical compression test of a model device was conducted. The load equipment was a hydraulic servo press machine. The maximum vertical load was 200 t, and maximum vertical displacement was 500 mm. A sketch of the loading equipment is shown in Fig. 6.

Three LRB100s were used in the test model. The inclination angle of the connection blocks was 10°. The friction blocks were made of polytetrafluoroethylene (PTFE), and the friction coefficient was 0.05. Three restrainers were positioned to make the sliding block move in the vertical direction, as shown in Fig. 7. The mechanical parameters of the LRB100s are listed in Table 2. The load cases are shown in Table 3.

Cases 1–3, 4–6, and 7–9 were classified into Groups 1, 2, and 3, respectively. In Group 1, the test model was loaded from the initial position. The target displacement was from 4 to 12 mm. In Group 2, the test model was loaded to static equilibrium (vertical load of 235 kN and displacement of 8 mm) and maintained for 15 min. Then, the test model was loaded at approximately equilibrium with an amplitude of 2 mm. In Group 3, the test model was loaded to

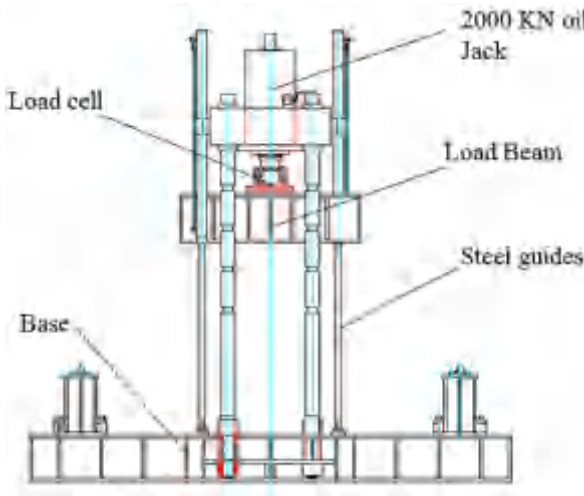


Fig. 6. Loading equipment.

approximately equilibrium, with an amplitude of 4 mm. The load rates of the cases in each group were 1, 2, and 3 mm=min, respectively. In each case, loading was conducted in four cycles.

The resultant oblique sliding of the friction block and compression-shear deformation of the inclined LRB are shown in Fig. 8.

Test Results

The hysteretic curves of Cases 1–9 are shown in Figs. 9(a–i), respectively. The hysteretic loops are asymmetric and spindle shaped, and the curves for each group are similar. The curves in Groups 2 and 3 were normalized, and the initial values were removed. The postyield loading and unloading stiffnesses are significantly different. The curves of Group 2 [Figs. 9(d–f)] have an approximately asymmetric quadrangle shape. In the curves of Groups 1 [Figs. 9(a–c)] and 3 [Figs. 9(g–i)], the postyield stiffness increased more than those in Group 2 due to the hardening effect of the rubber when the vertical displacement was larger than 10 mm. Some gaps formed between the actuator and the device in the very beginning of the test for Case 1, so the actual displacement of Case 1 is 11.2 mm.

The mechanical properties obtained from the test results are listed in Table 4. In Groups 1 and 3, the loading stiffness values were obtained before the hardening stage. The corresponding theoretical values of the mechanical properties can be determined from

Table 2. Mechanical parameters of test LRB100

Parameter	Value
Diameter (mm)	100
Total rubber thickness (mm)	14.3
First shape factor	19.23
Second shape factor	6.99
Vertical stiffness, K_v (kN=mm)	346.07
Postyield stiffness, K_d (kN=mm)	0.296
Yielding load, Q_d (kN)	1.616

Table 3. Load cases

Group	Case	Target displacement (mm)	Load speed (mm=min)	Cycles
1	1	4 – 12	1	4
	2	4 – 12	2	4
	3	4 – 12	3	4
2	4	8 ± 2	1	4
	5	8 ± 2	2	4
	6	8 ± 2	3	4
3	7	8 ± 4	1	4
	8	8 ± 4	2	4
	9	8 ± 4	3	4

the proposed hysteretic model. A comparison of the theoretical and test results is shown in Table 5. The equivalent damping ratio is

$$H_{eq} = \frac{\Delta W}{4\pi \cdot W} \quad (19)$$

where ΔW = dissipated energy per cycle; and W = potential energy at the maximum displacement.

The theoretical and tested mechanical properties match well. The errors are basically less than 20%. The inclined LRBs in Groups 1 and 3 were hardened during the loading process, causing the error between the theoretical and test values of the postyield unloading stiffness to be slightly larger. This difference is because the unloading stiffness of the LRB would be lower after the hardening effect is expressed. The larger the hardening deformation, the lower the unloading stiffness (Liu 2003). The effect of hardening on the mechanical behavior of the 3D OSFSI and dynamic response is to be discussed in further research.

The theoretical and test hysteretic curves are shown in Fig. 10. The theoretical and test curves match well, especially during the postyield process. The error during the unloading process is



Fig. 7. Test model of an 3D isolator.



Fig. 8. Oblique sliding of the inclined LRB.

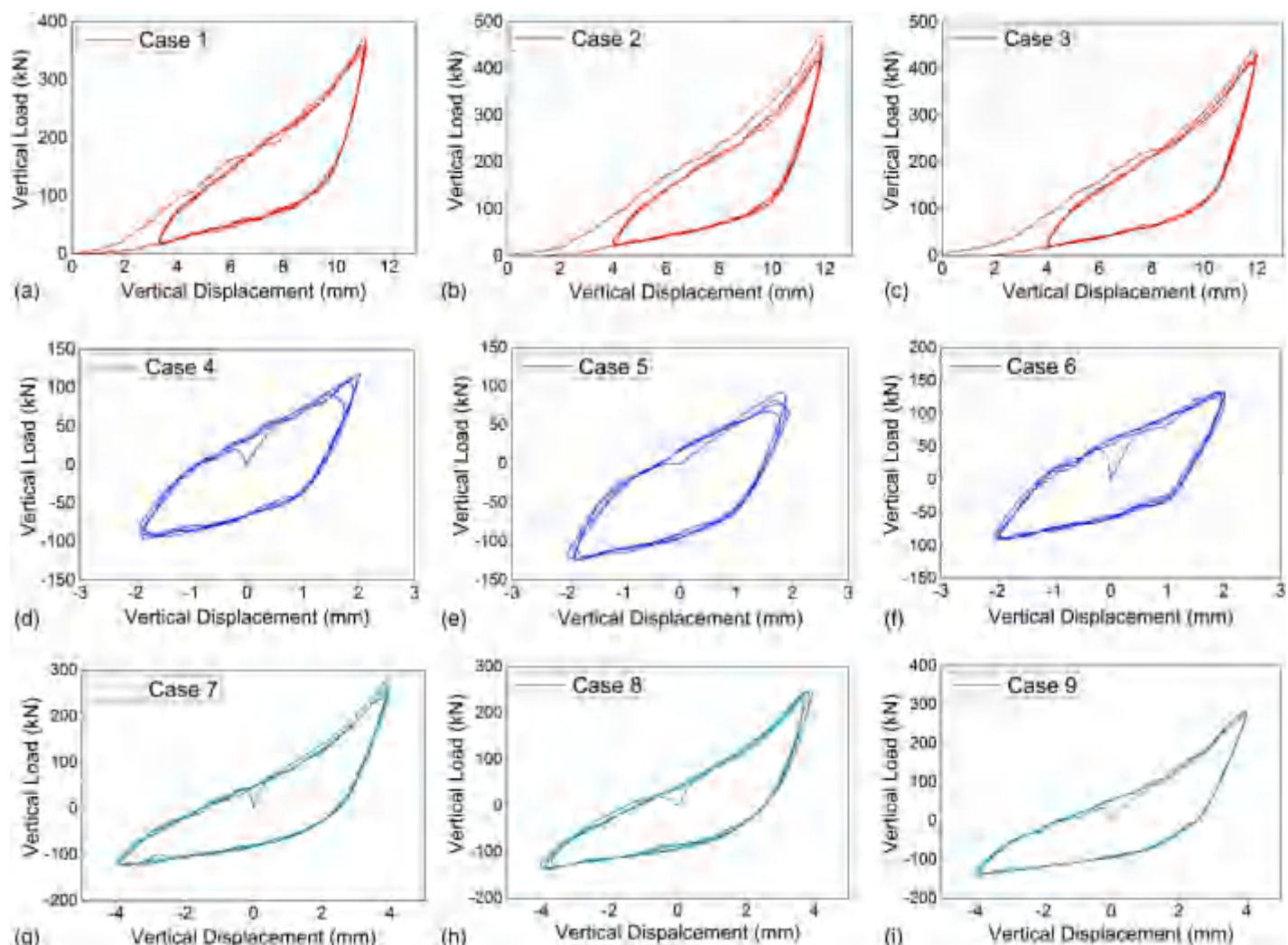


Fig. 9. Hysteretic curve of the different cases: (a) Case 1 (displacement 0–12 mm, load rate 1 mm=min); (b) Case 2 (displacement 0–12 mm, load rate 2 mm=min); (c) Case 3 (displacement 0–12 mm, load rate 3 mm=min); (d) Case 4 (displacement 8 ± 2 mm, load rate 1 mm=min); (e) Case 5 (displacement 8 ± 2 mm, load rate 2 mm=min); (f) Case 6 (displacement 8 ± 2 mm, load rate 3 mm=min); (g) Case 7 (displacement 8 ± 4 mm, load rate 1 mm=min); (h) Case 8 (displacement 8 ± 4 mm, load rate 2 mm=min); and (i) Case 9 (displacement 8 ± 4 mm, load rate 3 mm=min).

mainly caused by the hardening effect. The preyield stiffness was simply assumed to be 10–15 times the postyield stiffness, which is a simplified simulation method. However, the preyield stiffness is actually determined by the yielding force and lateral

stiffness of rubber. The vertical load influences the yielding force of the LRB (Liu 2003). Therefore, there are some errors of preyield stiffness. More adequate refinement will be explored in future research.

Table 4. Mechanical properties of the 3D OSFSI

Group	Case	Vertical yielding load (kN)	Postyield loading stiffness (kN=mm)	Postyield unloading stiffness (kN=mm)
1	1	49	34	13
	2	54	38	14
	3	52	40	14
2	4	38	39	17
	5	20	41	18
	6	58	41	21
3	7	54	35	16
	8	39	40	13
	9	50	38	14

The proposed mechanical model can efficiently simulate the vertical mechanical properties of the 3D OSFSI.

Parametric Analysis of the Mechanical Properties

The vertical mechanical properties of the 3D OSFSI mainly depend on the inclination angle, friction coefficient, and properties of the inclined LRBs. The variation in the mechanical properties with different parameter values can be obtained according to proposed theoretical model in the previous section.

Effect of Inclination Angle and Friction Coefficient

The calculation model is based on a device in which three LRB600s are used as the inclined LRBs. The geometry and mechanical properties of the selected LRB600s are shown in Table 6.

Figs. 11(a and b) show the variation in the vertical postyield loading stiffness and unloading stiffness with the inclination angle, respectively. The vertical stiffness of the 3D OSFSI decreases with increasing inclination angle. This vertical stiffness varies dramatically when the inclination angle is lower than 20° and slightly when the inclination angle is larger than 20°.

Table 5. Comparison of the theoretical and test results

Parameter	Theory value	Groups 1 and 3		Group 2	
		Average test value	Error (%)	Average test value	Error (%)
Vertical yielding load (kN)	40.09	49	20	38	5
Postyield stiffness, K_{dL-V} (kN=mm)					
Loading process	39.59	38	4	40	1
Unloading process	22.48	14	38	19	15
Equivalent damping ratio with amplitude of 2 mm	20.54%	—	—	21.6%	5

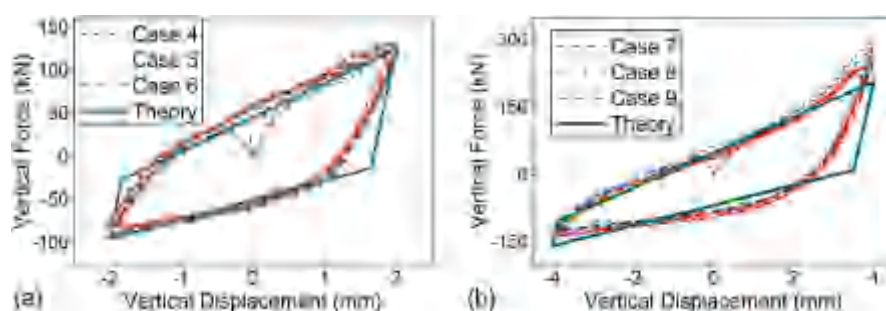


Fig. 10. Comparison of the theoretical curves and test curves with an amplitude of (a) 2 mm; and (b) 4 mm.

The variation in the ratio of the vertical postyield loading and unloading stiffnesses is shown in Fig. 11(c). When the friction coefficient is 0, the loading and unloading stiffnesses remain the same, and the mechanical model degenerates into a conventional bilinear model. When friction exists, the loading stiffness is greater. The influence of friction reduces with increasing inclination angle.

The variations in the maximum vertical load and vertical yielding load with inclination angle are displayed in Figs. 11(d and e), respectively. The maximum vertical load is defined as the vertical load when the shear strain of the inclined LRB is 300%. The maximum vertical load and vertical yielding load decrease with increasing inclination angle and decreasing friction coefficient. The influence of the friction reduces with increasing inclination angle.

The pressure of the inclined LRB when its shear strain is 100% is presented in Fig. 11(f). The pressure increases with the friction coefficient. The pressure decreases and the influence of the friction reduces with increasing inclination angle. The highest pressure for inclination angles between 10° and 45° is lower than 10 MPa.

Effect of the Inclined LRB

The properties of the inclined LRB depend on the shear modulus of the rubber and the shape factors of the rubber bearing (Architectural Society of Japan 2006). The shear modulus and shape factors of the selected LRB600 are defined as different values, and the variation is evaluated. The shape factors of LRB can be calculated as follows (Architectural Society of Japan 2006):

$$S_1 = \frac{\pi D^2 = 4}{\pi D t_R} = \frac{D}{4 t_R} \quad (20)$$

$$S_2 = \frac{D}{n t_R} \quad (21)$$

where D = diameter of the LRB; t_R = thickness of each rubber sheet; and n = number of rubber sheets.

Fig. 12(a) shows the variation in the vertical postyield loading stiffness with the first shape factor. The inclination angle, friction

Table 6. Geometry and mechanical properties of the LRB600

Property	Value
Diameter (mm)	600
Lead core diameter (mm)	100
Shear modulus (MPa)	0.4
First shape factor, S_1	30
Second shape factor, S_2	5
Vertical stiffness, K_v (kN/mm)	2,203
Postyield stiffness, K_d (kN/mm)	0.916
Yielding load, Q_d (kN)	84.82

coefficient, and second shape factor were defined as 15° , 0.05, and 5, respectively. When S_1 is less than 15, the stiffness increases with increasing S_1 . When S_1 is greater than 15, the stiffness remains approximately unchanged. The stiffness of the 3D OSFSI increases with the shear modulus.

The variation in the vertical postyield loading stiffness with the second shape factor is presented in Fig. 12(b). The inclination

angle, friction coefficient, and first shape factor are assumed to be 15° , 0.05 and 30, respectively. The vertical stiffness increases linearly with S_2 . The variation slope increases with S_2 .

The variation in the maximum vertical displacement with the inclination angle and second shape factor is displayed in Fig. 12(c). The maximum vertical displacement is defined as the vertical displacement when the shear strain of the inclined LRB is 300%. The friction coefficient and first shape factor were defined as 0.05 and 30, respectively. The maximum displacement increases with increasing inclination angle and decreasing second shape factor. The variation slope increases with decreasing second shape factor.

In general, the vertical mechanical properties of the 3D OSFSI are affected by the inclination angle, friction coefficient, and second shape factor of the inclined LRBs. The 3D OSFSI has a stronger deformation capacity and lower vertical stiffness when the inclination angle is larger. Rational parameters should be selected to meet both the deformation capacity and stiffness demands when designing such systems.

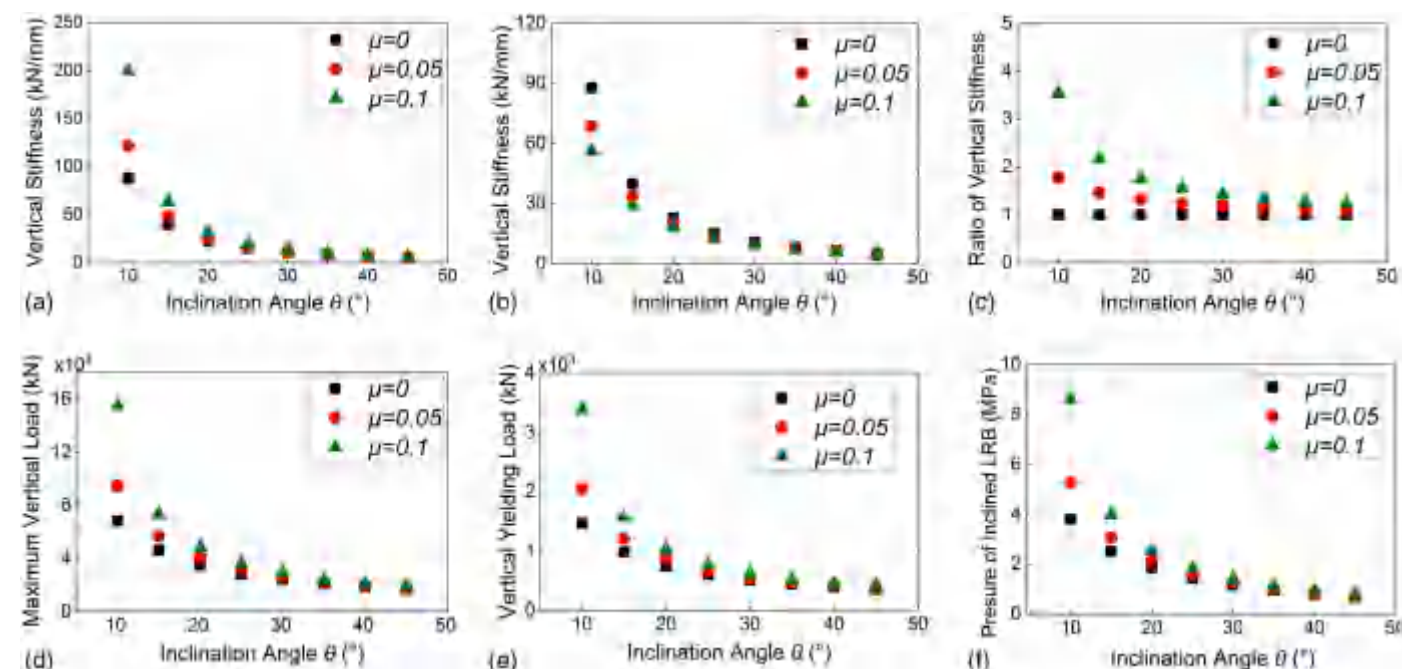


Fig. 11. Variation in the mechanical properties with inclination angle and friction coefficient: (a) variation in postyield loading stiffness with inclination angle; (b) variation in postyield unloading stiffness with inclination angle; (c) variation in loading and unloading stiffness ratio with inclination angle; (d) variation in maximum vertical load with inclination angle; (e) variation in vertical yielding load with inclination angle; and (f) variation in LRB pressure with inclination angle when the shear strain is 100%.

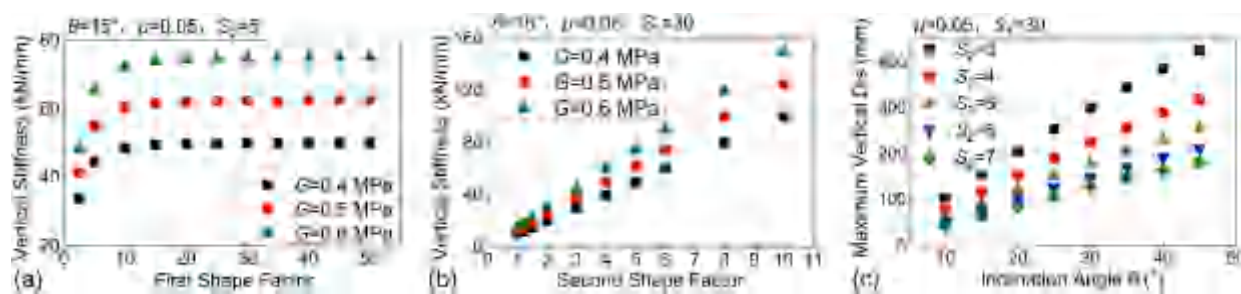


Fig. 12. Variation in the mechanical properties and shape factors: (a) variation in postyield loading stiffness with first shape factor; (b) variation in postyield loading stiffness with second shape factor; and (c) variation in maximum vertical displacement with second shape factor and inclination angle.

Dynamic Response Analysis

Structural Model and Input Ground Motions

A single-degree-of-freedom (SDOF) model of the substructure of an actual NPP structure was established using MATLAB. The calculation and hysteretic models of the isolation layer are shown in Fig. 13. The structural weight and static deformation were removed

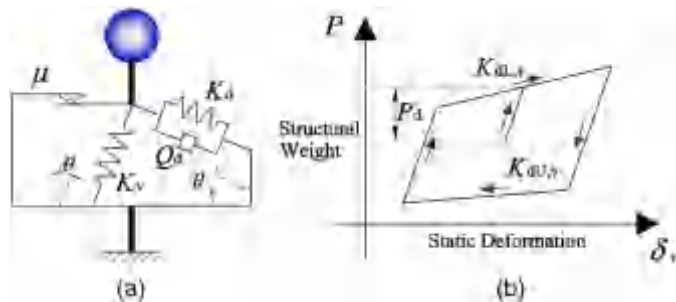


Fig. 13. SDOF model using the 3D OSFSI: (a) calculation model; and (b) hysteretic model.

Table 7. Mechanical parameters of the calculation model

Parameter	Value
Structure mass (m)	178.7
Components of the 3D OSFSI	
Number of 3D OSFSI	1
Diameter of the inclined LRBs (mm)	300
Number of inclined LRBs	3
Inclination angle (degrees)	20
Friction coefficient	0.05
Vertical properties of the 3D OSFSI	
Isolation period ^a (s)	1.2
First-order stiffness of the 3D OSFSI, K_v (kN-mm)	66
Postyield loading stiffness, $K_{dL,V}$ (kN-mm)	5.55
Postyield unloading stiffness, $K_{dU,V}$ (kN-mm)	4.22
Yield load, P_d (kN)	138
Horizontal bearing	
Diameter of horizontal LRB (mm)	600
Number of horizontal LRB	1
Vertical stiffness (kN-mm)	3,735
Fixed base	
Vertical frequency (Hz)	120

^aIsolation period is calculated using the average value of the postyield loading and unloading stiffnesses.

in the hysteretic model. The mechanical properties of the isolation layer can be obtained through Eqs. (15)–(17). The mechanical parameters of the isolator are listed in Table 7.

Three ground motions were selected in this study. The motions were generated artificially and are consistent with the RG1.60 response spectrum (NRC 2014). The input peak ground accelerations (PGAs) are 0.3 and 0.6 g. Selected waves and response spectra are displayed in Fig. 14.

Seismic Response

The vertical acceleration responses of the superstructure with 0.3 and 0.6 g PGA inputs are shown in Table 8. The peak vertical acceleration of the vertical isolation structure is lower than the PGA, whereas the horizontal isolation structure and fixed base structure amplify the peak vertical acceleration. The amplification factor of the vertical acceleration for the vertical isolation structure is approximately 0.70. In addition, those for the horizontal isolation structure and fixed base structure are approximately 1.68 and 1.04, respectively.

When the PGA is 0.3 g, the vertical acceleration of the vertical isolation structure reduces by 36% compared with that of a fixed base structure and reduces by 60% compared with that of a horizontal isolation structure. When the PGA is 0.6 g, the vertical acceleration of the vertical isolation structure reduces by 29% compared with that of a fixed base structure and reduces by 56% compared with that of a horizontal isolation structure.

The vertical hysteretic curves of the vertical isolation structure are displayed in Fig. 15. The postyield loading stiffness is greater than the unloading stiffness due to friction. The curves have an asymmetric quadrangle shape, which is similar to the shape of the curves from the test results. The vertical displacement of the isolation layer with a 0.6 g PGA is 3.36 times that with a 0.3 g PGA. The axial force with a 0.6 g PGA is 1.27 times that with a 0.3 g PGA.

Table 8. Vertical peak acceleration of the superstructure (m/s^2)

Input	Vertical isolation structure	Horizontal isolation structure	Fixed base structure
0.3 g			
Wave 1	2.08	5.46	3.15
Wave 2	2.16	5.14	3.19
Wave 3	1.77	4.54	3.02
0.6 g			
Wave 1	3.96	10.91	6.30
Wave 2	4.65	10.27	6.39
Wave 3	4.59	9.09	6.03

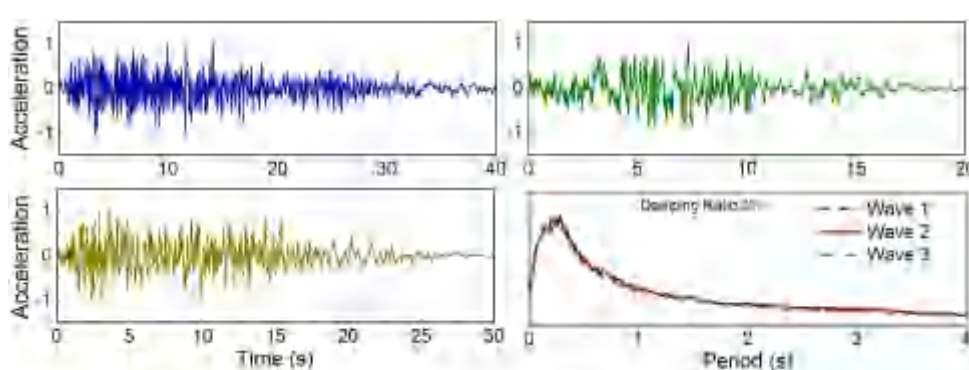


Fig. 14. Selected waves and response spectra.

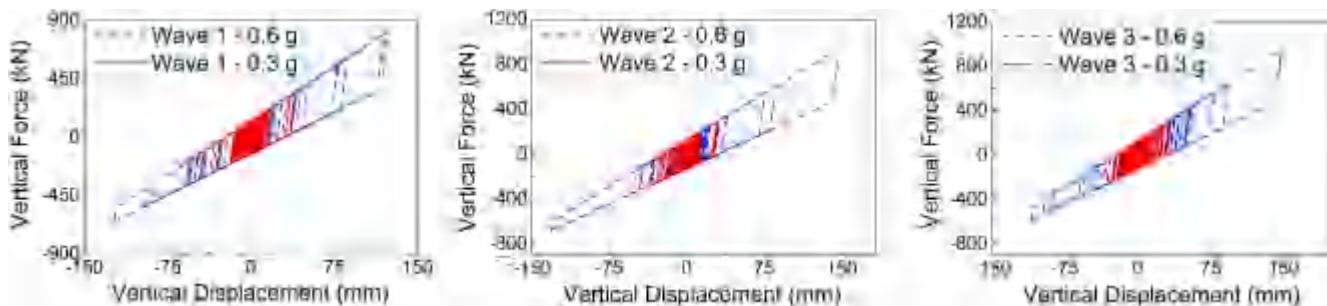


Fig. 15. Vertical hysteretic curves of the vertical isolation structure. The static vertical load is removed, and the vertical displacement is around static equilibrium.

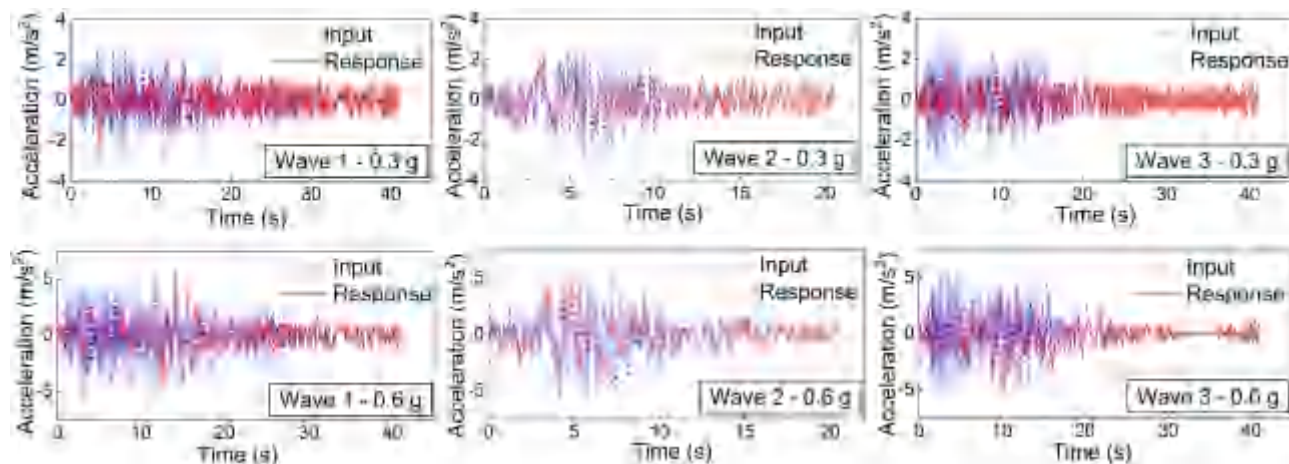


Fig. 16. Vertical acceleration response of the vertical isolation structure.

The vertical acceleration time history of the superstructure is shown in Fig. 16.

Comparison with Different Friction Coefficients

The structural responses with different friction coefficients are listed in Table 9. With an increasing friction coefficient, the vertical acceleration of the superstructure and the axial force of the isolation layer increase, whereas the vertical displacement decreases.

With Wave 1 input, when the friction coefficient increases by 0.05, the vertical acceleration increases by 10%, the axial force increases by 2%, and the vertical displacement decreases by 7%. When the friction coefficient increases by 0.1, the vertical acceleration increases by 22%, the axial force increases by 4%, and the vertical displacement decreases by 14%. The vertical acceleration and displacement are sensitive to friction, whereas the axial force is not because the axial force is determined by the seismic input and self-weight.

The vertical hysteretic curves with different friction coefficients are shown in Fig. 17. With an increasing friction coefficient, the loading stiffness increases, the unloading stiffness decreases, the displacement of the isolation layer decreases, and the axial force of the isolation layer increases.

The energy curves with different friction coefficients are presented in Fig. 18. The vertical isolation layer can sufficiently isolate the seismic input, decreasing the energy absorbed by the

Table 9. Structural response with different friction coefficients

Input	Property	Friction coefficient		
		0	0.05	0.1
Wave 1-0.3 g	Peak acceleration ($m=s^2$)	1.78	2.08	2.37
	Axial force ^a (kN)	2,105	2,159	2,210
	Displacement (mm)	43.7	43.1	41.6
Wave 1-0.6 g	Peak acceleration ($m=s^2$)	4.49	4.62	5.00
	Axial force (kN)	2,589	2,613	2,675
	Displacement (mm)	145.0	126.0	112.3

^aAxial force includes the structural weight and earthquake force. Positive values indicate pressure.

superstructure. The isolation system with a larger friction coefficient inputs and dissipates more energy. The input energy is defined as the sum of the energy dissipated by the isolation layer and absorbed by the superstructure. The damping ratio of the superstructure is defined as 7% (Li et al. 2005). The energy absorbed by the superstructure of the different isolation systems is approximate.

The proposed system can effectively reduce structural responses. Varied results can be achieved using different LRBs and inclination angles. An analysis of the actual NPP structure will be conducted and the optimized parameters will be explored in subsequent research. In addition, the 3D responses of nuclear equipment will be considered.

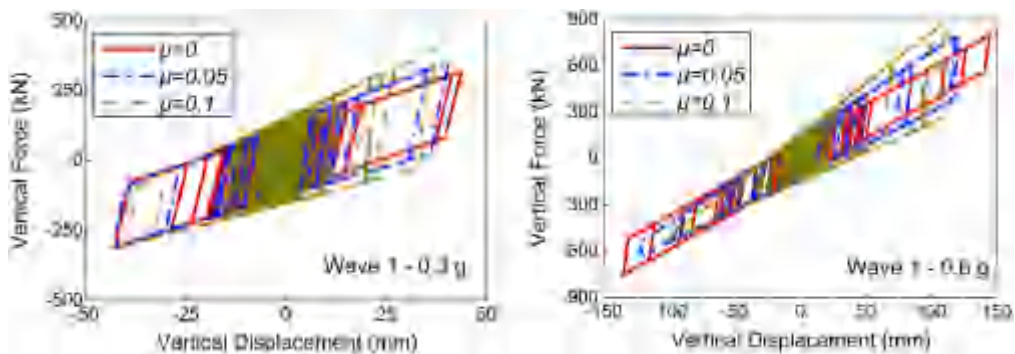


Fig. 17. Vertical hysteretic curves with different friction coefficients.

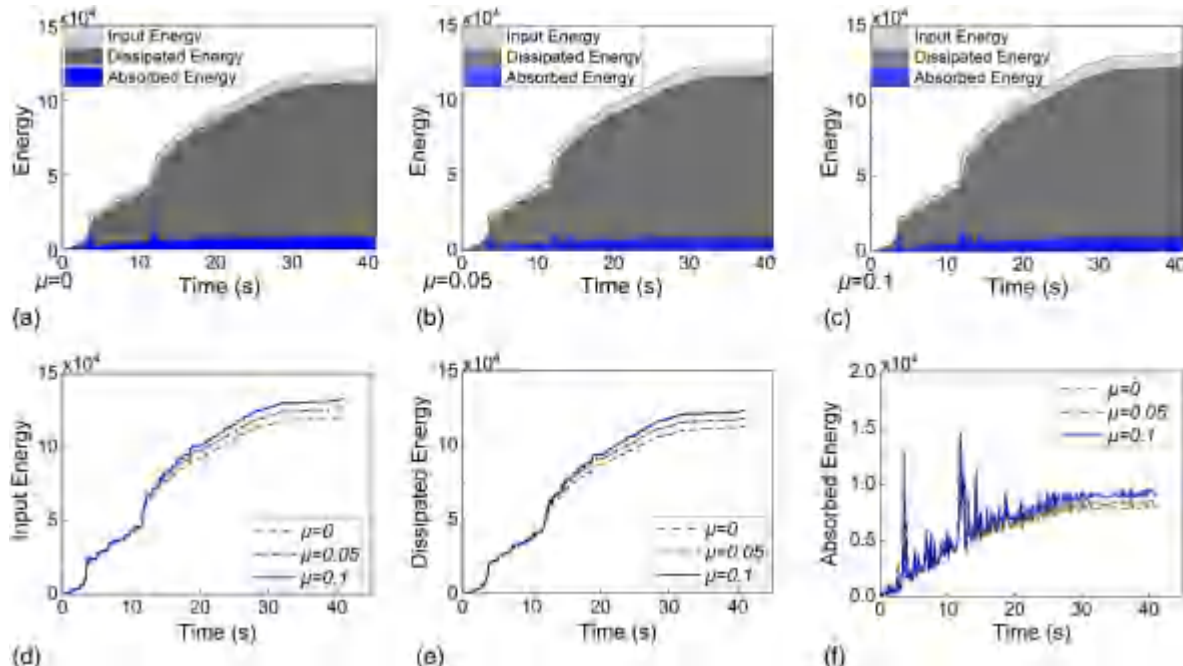


Fig. 18. Energy curves with different friction coefficients under the Wave 1 PGA with 0.3 g input: (a) energy time history without friction; (b) energy time history with a friction coefficient of 0.05; (c) energy time history with a friction coefficient of 0.1; (d) comparison of input energy; (e) comparison of dissipated energy; and (f) comparison of absorbed energy.

Conclusions

In this paper, a new kind of 3D OSFSI was proposed, and a non-parallel oblique hysteretic model was introduced. A static test and dynamic response analysis were conducted. The main conclusions are as follows:

- The proposed 3D OSFSI can transform vertical deformation into oblique sliding of the inclined LRBs. This system can balance a high supporting capacity and low vertical stiffness to realize 3D isolation. The 3D OSFSI has a reasonable structure and clear load path.
- An asymmetric hysteretic model of the 3D OSFSI was proposed. The calculation formulas of the proposed model were presented based on a force analysis of the proposed device. The postyield loading and unloading stiffnesses are different due to friction sliding. The hysteretic loop has the shape of an asymmetric quadrangle.
- A quasistatic test was conducted. The vertical hysteretic curve of the 3D OSFSI is asymmetric and spindle shaped. The postyield

loading stiffness is approximately 39 kN/mm. The device has a stable supporting capacity and hysteretic behavior. The equivalent damping ratio is approximately 21.6% with an amplitude of 2 mm. A dissimilarity in the postyield loading and unloading stiffnesses was observed.

- The proposed hysteretic model results were compared with test results. The mechanical properties from the theoretical and test results match well; the errors are generally less than 20%. The proposed mechanical model can efficiently simulate the vertical behavior of the proposed system.
- A parametric analysis of the 3D OSFSI was conducted. The inclination angle, friction coefficient, and second shape factor of the inclined LRB strongly affect the vertical properties. The vertical stiffness decreases, the deformation capacity increases, and load capacity decreases with increasing inclination angle. The 3D OSFSI has a higher stiffness and stronger load capacity with higher friction coefficients.
- A dynamic response analysis of a SDOF NPP structure was performed. The shape of the hysteretic curves is similar to those

from the test results. The vertical acceleration response of the vertical isolation structure reduces by 33% compared with that of a fixed base structure and reduces by 58% compared with that of a horizontal isolation structure. The vertical isolation layer can sufficiently isolate the seismic input. With an increasing friction coefficient, the vertical acceleration of the superstructure and the axial force of the isolation layer increase, whereas the vertical displacement decreases.

Acknowledgments

This work was supported by the National Natural Science Foundation of China (Grant No. 51478257), Natural Science Foundation of Shanghai (Grant No. 15ZR1416200), and Research Fund for the Doctoral Program of Higher Education of China (Grant No. 20133108110024). The authors also want to acknowledge the Shanghai Nuclear Engineering Research & Design Institute Co., Ltd. for providing the ground motions used in this project.

References

- Architectural Society of Japan. 2006. Recommendation for the design of base isolated buildings. [In Chinese.] Translated by W. G. Liu. Beijing: Seismological Press.
- Bertero, V. V., S. A. Mahin, and R. A. Herrera. 1978. "Aseismic design implications of near-fault San Fernando earthquake records." *Earthquake Eng. Struct. Dyn.* 6 (1): 31–42. <https://doi.org/10.1002/eqe.4290060105>.
- Bozorgnia, Y., K. W. Campbell, and M. Niazi. 2000. "Observed spectral characteristics of vertical ground motion recorded during worldwide earthquakes from 1957 to 1995." In Proc., 12th World Conf. on Earthquake Engineering. Auckland, New Zealand: New Zealand National Society for Earthquake Engineering.
- Chan, G. K., and J. M. Kelly. 1988. "A simple mechanical model for elastomeric bearings used in base isolation." *Int. J. Mech. Sci.* 30 (12): 933–943. [https://doi.org/10.1016/0020-7403\(88\)90075-6](https://doi.org/10.1016/0020-7403(88)90075-6).
- Chopra, A. K. 2005. Dynamics of structures: Theory and applications to earthquake engineering. [In Chinese.] Translated by L. L. Xie and D. G. Lv. Beijing: Higher Education Press.
- Fujita, S., E. Kato, A. Kashiwazaki, I. K. Shimoda, and K. O. Sasaki. 1996. "Shake table tests on three-dimensional vibration isolation system comprising rubber bearing and oil spring." In Proc., 11th World Conf. on Earthquake Engineering. Acapulco, Mexico: Mexico Society of Seismic Engineers.
- Garevski, M. A., J. M. Kelly, and N. V. Zisi. 2000. "Analysis of 3D vibrations of the base isolated school building 'Pestalozzi' by analytical and experimental approach." In Proc., 12th World Conf. on Earthquake Engineering. Auckland, New Zealand: New Zealand National Society for Earthquake Engineering.
- Han, X., C. A. Kelleher, G. P. Warn, and T. Wagener. 2013. "Identification of the controlling mechanism for predicting critical loads in elastomeric bearings." *J. Struct. Eng.* 139 (12): 04013016. [https://doi.org/10.1061/\(ASCE\)ST.1943-541X.0000811](https://doi.org/10.1061/(ASCE)ST.1943-541X.0000811).
- Haringx, J. A. 1948. "On highly compressible helical springs and rubber rods and their application for vibration-free mountings." *Philips Res. Rep.* 3: 401–449.
- Hossein, M., and T. Kabeyasawa. 2004. "Effect of infill masonry walls on the seismic response of reinforced concrete buildings subjected to the 2003 Bam earthquake strong motion: A case study of Bam Telephone Center." [In Japanese.] *Bull. Earthquake Res. Inst. Univ. Tokyo* 79 (3–4): 133–156.
- Indirli, M., C. Nunziata, F. Romenelli, and F. Vaccari. 2009. "Design and placing of an innovative 3D-isolation system under the Herculaneum Roman Ship." In Proc., PROHITECH Conf.—Protection of Historical Buildings, 681–687. Berlin: Springer.
- Inoue, K., M. Morishita, and T. Fujita. 2004. "Development of three-dimensional seismic isolation technology for next generation nuclear power plant in Japan." In Proc., ASME/JSME 2004 Pressure Vessels and Piping Conf. 29–34. New York: ASME.
- Kato, A., K. Umeki, M. Morishita, T. Fujita, and S. Midorikawa. 2002. "A large scale ongoing R&D project on three-dimensional seismic isolation for FBR in Japan." In Proc., ASME 2002 Pressure Vessels and Piping Conf., 1–9. New York: ASME.
- Kelly, J. M., I. G. Buckle, and C. G. Koh. 1987. "Mechanical characteristics of base isolation bearings for a bridge deck model test." UCB/EERC-86/11. Berkeley, CA: Earthquake Engineering Research Center, Univ. of California at Berkeley.
- Lee, Y., Y. S. Ji, W. Han, S. Choi, and S. G. Cho. 2014. "Shaking table test of vertical isolation device." *Int. J. Environ. Sci. Dev.* 5 (1): 5–7.
- Li, X., Z. Zhou, H. Yu, R. Wen, D. Lu, M. Huang, Y. Zhou, and J. Cu. 2008. "Strong motion observations and recordings from the great Wenchuan earthquake." *Earthquake Eng. Eng. Vibr.* 7 (3): 235–246. <https://doi.org/10.1007/s11803-008-0892-x>.
- Li, Z. X., Z. C. Li, and W. X. Shen. 2005. "Sensitivity analysis for floor response spectra of nuclear reactor buildings." [In Chinese.] *Nucl. Power Eng.* 26 (1): 44–50.
- Liu, W. G. 2003. Mechanics properties of rubber bearings and earthquake response analysis of isolated structure. [In Chinese.] Beijing: Beijing Univ. of Technology.
- Masaki, M., K. Seiji, M. Satoshi, and F. Minoru. 2003. "Development of 3D seismic isolation technology for advanced nuclear power plant application." In Proc., Int. Conf. on Advanced Nuclear Power Plants and Global Environment (GENES4/ANP2003). Kyoto, Japan: Atomic Energy Society of Japan.
- Morishita, M., K. Inoue, and T. Fujita. 2004. "Development of three-dimensional seismic isolation systems for fast reactor application." *J. J. Assoc. Earthquake Eng.* 4 (3): 305–310. https://doi.org/10.5610/jae.4.3_305.
- Nagarajaiah, S., and K. Ferrell. 1999. "Stability of elastomeric seismic isolation bearings." *J. Struct. Eng.* 125 (9): 946–954. [https://doi.org/10.1061/\(ASCE\)0733-9445\(1999\)125:9\(946\)](https://doi.org/10.1061/(ASCE)0733-9445(1999)125:9(946)).
- NRC (US Nuclear Regulatory Commission Office of Nuclear Regulatory Research). 2014. Regulatory guide 1.60 design response spectra for seismic design of nuclear power plants. Rockville, MD: NRC.
- Ogiso, S., K. Nakamura, M. Suzuki, and S. Moro. 2003. "Development of 3D seismic isolator using metallic bellows." In Proc., Transactions of the 17th Int. Conf. on Structural Mechanics in Reactor Technology (SMiRT 17). Prague, Czech Republic: State Office for Nuclear Safety of the Czech Republic.
- Ou, J. P., and J. F. Jia. 2010. "Seismic performance of a novel 3D isolation system on continuous bridges." In Vol. 7643 of Active and Passive Smart Structures and Integrated Systems. Bellingham, WA: International Society of Photo-Optical Instrumentation Engineers.
- Papazoglou, A. J., and A. S. Elnashai. 1996. "Analytical and field evidence of the damaging effect of vertical earthquake ground motion." *Earthquake Eng. Struct. Dyn.* 25 (10): 1109–1137. [https://doi.org/10.1002/\(SICI\)1096-9845\(199610\)25:10<1109::AID-EQE604>3.0.CO;2-0](https://doi.org/10.1002/(SICI)1096-9845(199610)25:10<1109::AID-EQE604>3.0.CO;2-0).
- Ryan, K. L., J. M. Kelly, and A. K. Chopra. 2006. "Formulation and implementation of a lead-rubber bearing model including material and geometric nonlinearities." In Analysis and Computation Specialty Conferenc at Structures, 1–13. Reston, VA: ASCE.
- Sanchez, J., A. Masroor, G. Mosqueda, and K. Ryan. 2013. "Static and dynamic stability of elastomeric bearings for seismic protection of structures." *J. Struct. Eng.* 139 (7): 1149. [https://doi.org/10.1061/\(ASCE\)ST.1943-541X.0000660](https://doi.org/10.1061/(ASCE)ST.1943-541X.0000660).
- Sawa, N., S. Kajii, and K. Umeki. 2002. "Study on 3D seismic isolation applied to advanced power reactor: Using hydraulic cylinder: No. 1." [In Japanese.] In Vol. 2002 of Proc., Dynamics and Design Conf. Tokyo: Japan Society of Mechanical Engineers.
- Shimada, T., et al. 2010. "420 development study on hydraulic 3D seismic isolation system applied to advanced nuclear power plant: Verification of characteristics in high pressure condition on the rocking suppression system." [In Japanese.] In Proc., Dynamics and Design Conf. Tokyo: Japan Society of Mechanical Engineers.
- Suhara, J., T. Hagiwara, Y. Okada, R. Matsumoto, K. Takahashi, and M. Fushimi. 2004. "104 study on three-dimensional seismic isolation

- system applied to advanced nuclear power plants: Rolling seal type air spring." [In Japanese.] In Proc., Dynamics and Design Conf. Tokyo: Japan Society of Mechanical Engineers.
- Tomizawa, T., O. Takahashi, H. Aida, J. Suhara, M. Saruta, K. Okada, Y. Tsuyuki, T. Suzuki, and T. Fujita. 2012. "Vibration test in a building named 'Chisukan' using three-dimensional seismic isolation system." In Proc., 15th World Conf. on Earthquake Engineering (15WCEE). Lisboa, Portugal: Portuguese Society for Earthquake Engineering.
- UDC (Ministry of housing and Urban-Rural Development of China). 2010. Code for seismic design of buildings. [In Chinese.] GB50011-2010. Beijing: UDC.
- Ueda, M., K. Ohmata, R. Yamagishi, and J. Yokoo. 2007. "Vertical and three-dimensional seismic isolation tables with bilinear spring force characteristics: For which a Λ -shaped link mechanism is used (mechanical systems)." [In Japanese.] Trans. J. Soc. Mech. Eng. 73 (735): 2932–2939. <https://doi.org/10.1299/kikaic.73.2932>.
- Vu, B., M. Unal, G. P. Warn, and A. M. Memari. 2014. "A distributed flexibility and damping strategy to control vertical accelerations in base-isolated buildings." Struct. Control Health Monit. 21 (4): 503–521. <https://doi.org/10.1002/stc.1580>.
- Warn, G. P., and A. S. Whittaker. 2008. "Vertical earthquake loads on seismic isolation systems in bridges." J. Struct. Eng. 134 (11): 1696–1704. [https://doi.org/10.1061/\(ASCE\)0733-9445\(2008\)134:11\(1696\)](https://doi.org/10.1061/(ASCE)0733-9445(2008)134:11(1696)).
- Warn, G. P., A. S. Whittaker, and M. C. Constantinou. 2007. "Vertical stiffness of elastomeric and lead-rubber seismic isolation bearings." J. Struct. Eng. 133 (9): 1227–1236. [https://doi.org/10.1061/\(ASCE\)0733-9445\(2007\)133:9\(1227\)](https://doi.org/10.1061/(ASCE)0733-9445(2007)133:9(1227)).
- Weisman, J., and G. P. Warn. 2012. "Stability of elastomeric and lead-rubber seismic isolation bearings." J. Struct. Eng. 138 (2): 215–223. [https://doi.org/10.1061/\(ASCE\)ST.1943-541X.0000459](https://doi.org/10.1061/(ASCE)ST.1943-541X.0000459).
- Xue, Q. 2000. "Need of performance-based earthquake engineering in Taiwan: A lesson from the Chichi earthquake." Earthquake Eng. Struct. Dyn. 29 (11): 1609–1627. [https://doi.org/10.1002/1096-9845\(200011\)29:11<1609::AID-EQE977>3.0.CO;2-M](https://doi.org/10.1002/1096-9845(200011)29:11<1609::AID-EQE977>3.0.CO;2-M).
- Yabana, S., and A. Matsuda. 2000. "Mechanical properties of laminated rubber bearings for three-dimensional seismic isolation." In Proc., 12th World Conf. on Earthquake Engineering. Auckland, New Zealand: New Zealand National Society for Earthquake Engineering.
- Yang, J., and C. M. Lee. 2007. "Characteristics of vertical and horizontal ground motions recorded during the Niigata-ken Chuetsu, Japan earthquake of 23 October 2004." Eng. Geol. 94 (1): 50–64. <https://doi.org/10.1016/j.enggeo.2007.06.003>.
- Zhou, Z. G., J. Wong, and S. Mahin. 2016. "Potentiality of using vertical and 3D isolation systems in nuclear structures." Nucl. Eng. Technol. 48 (5): 1237–1251. <https://doi.org/10.1016/j.net.2016.03.005>.